Electronic transport properties of Janus Ge$_2$PAs monolayer: A prototype 2D metal–semiconductor–metal device

D. H. Ozbey ⓘ ; G. Ö. Sargin ⓘ ; V. Ongun Özçelik ⓘ ; E. Durgun ✉ ⓘ

Check for updates

View Online

Export Citation

AIP Publishing

Electronic transport properties of Janus Ge$_2$PAs monolayer: A prototype 2D metal–semiconductor–metal device

D. H. Ozbey,[1] 🆔 G. Ö. Sargin,[1,2] 🆔 V. Ongun Özçelik,[2,3] 🆔 and E. Durgun[1,a] 🆔

AFFILIATIONS

[1]UNAM—National Nanotechnology Research Center and Institute of Materials Science and Nanotechnology, Bilkent University, Ankara 06800, Turkey
[2]Faculty of Engineering and Natural Sciences, Sabanci University, Istanbul 34956, Turkey
[3]Materials Science and Nano Engineering Program, Sabanci University, Istanbul 34956, Turkey

[a]Author to whom correspondence should be addressed: durgun@unam.bilkent.edu.tr

ABSTRACT

The semiconductor industry's quest for miniaturization has driven the exploration of new materials and innovative designs. Among these, two-dimensional (2D) semiconductor materials have emerged as promising candidates due to their unique electrical conductivity and superior carrier transport properties, which address the limitations of conventional bulk semiconductors at the nanoscale. Understanding the electronic transport properties of 2D materials is essential for unlocking their full potential in emerging nanoelectronic applications. In this context, our study focuses on the transport characteristics of Janus Ge$_2$PAs monolayer-based metal–semiconductor–metal (MSM) devices. Utilizing DFT (density functional theory) simulations coupled with the nonequilibrium Green's function method, we explore the effects of external factors, such as channel length and electrode doping concentration on device performance in the ballistic region (sub-10 nm). By modeling two-probe MSM nanodevices, we analyze transmission coefficients [$T(E)$] under varying bias voltages and study the I–V characteristics' dependence on channel lengths and doping concentrations. Our findings provide valuable insights into the electronic transport properties of the Janus Ge$_2$PAs monolayer and offer guidance for the design and optimization of 2D material-based nanoelectronic devices.

I. INTRODUCTION

As the semiconductor industry advances, the prominence of microelectronic devices continues to grow, driven by the ongoing reduction in the feature size of individual transistors. This pursuit of miniaturization has fueled exponential growth in computing power over recent decades.[1] However, as device dimensions approach nanoscale, conventional bulk materials encounter intrinsic limitations, necessitating the development of novel materials and design paradigms to sustain and enhance technological advancements.[2] In this context, the exploration of two-dimensional (2D) semiconductor materials has emerged as a key area of scientific investigation.[3] Characterized by unique electrical conductivity and superior carrier transport properties, 2D materials present a promising solution to the challenges faced by conventional bulk semiconductors at the nanoscale.[4,5] With their high carrier mobility[6–8] enabling rapid charge transport and excellent thermal conductivity[9] facilitating efficient heat dissipation, these atomically thin materials exhibit remarkable electronic properties. The inherent characteristics make 2D materials highly promising candidates for the next-generation electronic devices, which require not only high-speed data processing but also enhanced thermal management to ensure device reliability and performance.

Given the significant influence of electronic transport properties on the operation and efficiency of vital electronic devices, such as field-effect transistors (FETs) and metal–oxide–semiconductor field-effect transistors (MOSFETs), it is crucial to understand the transport characteristics of 2D materials thoroughly.[10] This knowledge is essential to harness the full potential of 2D materials in emerging nanoelectronic applications. Consequently, intensive

research efforts have focused on discovering and characterizing 2D semiconductors with exceptional transport properties, particularly in terms of carrier mobilities.[11,12] Transition metal dichalcogenides (TMDs) have garnered considerable interest as some of the most promising 2D semiconductors in recent years.[13] However, their practical implementation is often limited by low carrier mobilities caused by inherent defects in their material structure.[14] This challenge has spurred interest in the fabrication of few-layered group IV–V binary compounds, which have become a new focal point for 2D materials research.[15–19] These materials, characterized by their low symmetries and distinctive bonding types in different directions, are anticipated to exhibit anisotropic electronic, mechanical, and optical properties.[20] Studies have confirmed the electronic anisotropy of group IV–V monolayers, particularly XAs (where X = Si or Ge), revealing that electron mobility is significantly higher in one direction, while hole mobility performs better in another.[21] Furthermore, theoretical research suggests that due to its low carrier effective mass, the carrier mobility of single-layer SiP is expected to surpass that of monolayer MoS_2.[22] Additionally, investigations have shown that monolayers of GeP and GeAs exhibit exceptional electron and hole mobilities, outperforming those of TMDs and highlighting their potential role in advanced semiconductor technologies.[23] Complementing these findings, recent literature details the computational design of 2D GeP-based electronic devices, demonstrating that introducing vacancies and strain can further enhance electrical performance.[24,25] Beyond binary monolayers, such as the aforementioned group IV–V materials, Janus monolayers within the realm of 2D materials have gained substantial attention, particularly following the successful synthesis of 2D ternary MoSSe.[26,27] In Janus monolayers, the introduction of a third element disrupts the out-of-plane mirror symmetry, leading to the emergence of novel physical properties or enhanced functionalities compared to their parent structures.[28–32] Additionally, the unique structural asymmetry of 2D Janus materials alters their defect dynamics, potentially mitigating the negative effects of defects and can exhibit higher defect tolerance compared to conventional TMDs.[30,33,34]

Recently, we have employed this approach to design the 2D Janus Ge_2PAs (also referred to as GePAs), predicting that this structure would demonstrate exceptionally high and anisotropic carrier mobility along with robust thermodynamic stability.[35] The distinct electronic behavior of 2D Ge_2PAs arises from the specific bonding environment of atoms along one of the in-plane directions, which enables carrier mobility that surpasses even the ultra-high mobility observed in few-layered black phosphorus.[36] Moreover, the Ge_2PAs monolayer exhibits a strong optical absorption coefficient in both the visible and near-infrared (NIR) regions of the spectrum, significantly enhancing its ability to harvest photons across a wide range of wavelengths. Its anisotropic nature, combined with high carrier mobility along a particular direction, facilitates the efficient transport of photo-generated carriers, minimizing recombination losses and enabling a fast photoresponse. These combined properties make the Ge_2PAs monolayer an ideal candidate for broad-spectrum photodetectors capable of operating effectively in the visible and NIR regions.[37]

While theoretical examinations based on density functional theory (DFT) provide valuable insights into the electronic properties of materials, it is imperative to assess the transport characteristics of devices fabricated with these materials for practical applications. The fundamental architecture, consisting of a semiconductor material sandwiched between two metal electrodes, is a common feature present in virtually every device system. Motivated by the promising properties of a Janus Ge_2PAs monolayer, we conduct DFT simulations combined with the Nonequilibrium Green's Function (NEGF) method to investigate the impact of external factors, such as channel length and electrode doping concentration, on the performance of Ge_2PAs-based two-terminal metal–semiconductor–metal (MSM) devices in the ballistic region (sub-10 nm). To begin with, we obtain the electronic band structure of the pristine monolayer. Subsequently, we model the two-probe MSM nanodevice and demonstrate the transmission coefficients ($[T(E)]$) of the devices under varying bias voltages. Next, we investigate the dependence of the I–V characteristics of the devices on different channel lengths and electrode doping concentrations. Finally, we explore the Schottky barrier (SB) heights and discuss their effect on carrier transport.

II. METHODS

The geometry optimization and electronic structure calculations were conducted using the DFT approach implemented in the Vienna *Ab initio* Simulation Package (VASP).[38,39] The generalized gradient approximation with the Perdew-Burke-Ernzerhof (GGA-PBE) formalism[40] was chosen to approximate the exchange-correlation functional. Ion–electron interactions were treated using the projected augmented wave method (PAW) with a plane-wave cutoff energy of 530 eV.[41] The Brillouin zone (BZ) was sampled with a $24 \times 4 \times 1$ k-point mesh centered at Γ using the Monkhorst–Pack scheme.[42] To eliminate artificial interactions, a vacuum space of approximately 15 Å was introduced, which was found to be sufficient. Van der Waals (vdW) interactions were described using the Grimme method (DFT-D3).[43] The lattice parameters and atomic positions were iteratively adjusted until the forces on the atoms were below 0.01 eV/Å, and the energy difference between consecutive steps was smaller than 10^{-5} eV.

The device model was constructed directly using the optimized structure, and simulations of the $T(E)$ and the I–V characteristics were conducted using the QuantumATK package.[44] QuantumATK provides a reliable framework for evaluating transport properties by integrating DFT calculations in conjunction with the Non-Equilibrium Green's Function (NEGF) technique.[45] The NEGF-DFT formalism was employed to model a two-probe system, which is divided into three regions: the left electrode (drain), the central region (channel), and the right electrode (source). The electrodes were modeled as semi-infinite periodic systems, with their properties were calculated using standard DFT techniques to define boundary conditions for the central region. The calculations began with an initial guess for the electron density, which was used to determine the effective potential (V_{eff}), including contributions from the Hartree and exchange-correlation terms. Using this effective potential, the Kohn–Sham Hamiltonian was constructed, and the Green's function for the central region was computed. The Green's function incorporated the coupling to the electrodes through self-energy terms (Σ^L and Σ^R). The density matrix was

09 December 2025 11:57:19

then derived from Green's function, accounting for the coupling matrices (self-energy contributions) and the Fermi–Dirac distributions of the electrodes. The electron density was iteratively updated from the density matrix until convergence was achieved for V_{eff} and charge density. Once the system was converged, the transmission function $[T(E)]$ was calculated.

In these simulations, the carrier transport direction was set along the x axis, with Monkhorst–Pack k-grid sampling specified as $201 \times 2 \times 1$. The atomic cores were represented using PseudoDojo pseudopotentials,[46] and a medium numerical basis was utilized for the expansion of the wave function. The density mesh cutoff energy was set to 105 Ry to balance computational efficiency and accuracy. The electrode temperature was maintained at 300 K. Bulk properties were assigned to the left and right electrodes, and the initial step in the device simulation involved conducting bulk calculations for each electrode with Dirichlet boundary conditions applied at both the left and right boundaries. Periodic boundary conditions were applied in the directions perpendicular to the electron transport directions.

The self-consistent solution for the transmission coefficient $[T(E, V_b)]$ under different biases (V_b) was obtained using the retarded Green's function,[47]

$$T(E, V_b) = Tr\big[G(E, V_b)\Gamma^L G^\dagger(E, V_b)\Gamma^R\big], \qquad (1)$$

where $\Gamma^{L(R)}$ is the broadening function of the left (right) electrode given by $\Gamma^{L(R)} = 1/i(\Sigma^{L(R)} - (\Sigma^{L(R)})^\dagger)$ with self-energy of the left (right) electrode $\Sigma^{L(R)}$. Applying a V_b across the device results in a shift of the chemical potentials of the left (μ_L) and right (μ_R) electrodes to $\mu_L = E_F + eV_b/2$ and $\mu_R = E_F - eV_b/2$, respectively. The current flow along the transport direction is then driven by the difference in chemical potential between the left and right electrodes. The current induced by a V_b, i.e., the I–V characteristics for the two-terminal system, was calculated using the Landauer–Büttiker formula within the framework of quantum transport formalism. This involves integrating $T(E, V_b)$ within the bias window, which ranges from $-eV_b/2$ to $+eV_b/2$,

$$I(V_b) = \frac{2e}{h} \int_{\mu_L}^{\mu_R} T(E, V_b)\big[f_L(E, V_b) - f_R(E, V_b)\big]dE, \qquad (2)$$

where $f_L(E, V_b)$ and $f_R(E, V_b)$ are the Fermi distribution of the left and right electrodes, respectively.

III. RESULTS AND DISCUSSION

A. Structural and electronic properties

This section explores the structural characteristics of the 2D Ge$_2$PAs monolayer, as initially proposed in our previous work.[35] Inspired by recent advancements in ternary monolayer synthesis[26,27] and the successful realization of 2D GeP[17] and GeAs,[19] we designed 2D Ge$_2$PAs by substituting arsenic atoms into the topmost layer of 2D GeP. Upon substitution, the Janus Ge$_2$PAs monolayer exhibits the monoclinic C_s point group (Cm space group), distinguished by broken symmetries, such as rotational and inversion symmetries, unlike the GeP and GeAs counterparts,
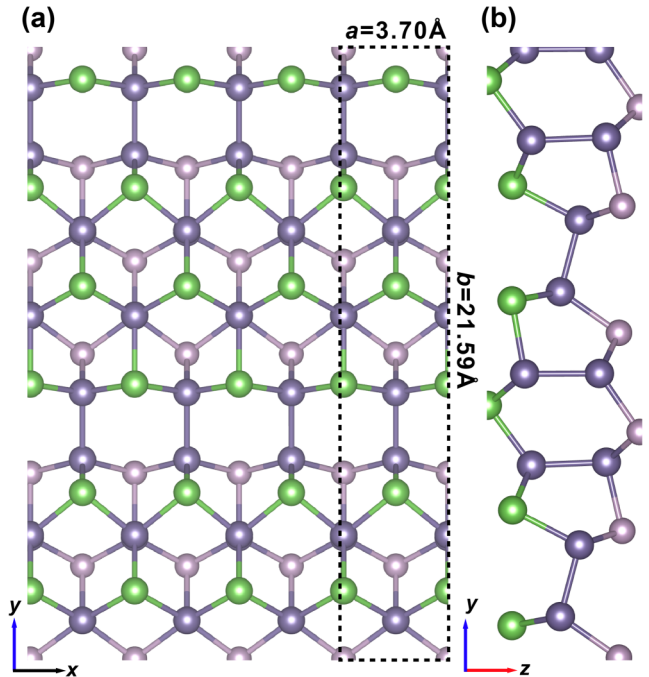
FIG. 1. (a) Top and (b) side views of a Janus Ge$_2$PAs monolayer. The dashed black rectangle denotes the unit cell. Germanium, phosphorus, and arsenic atoms are depicted as purple, pink, and green spheres, respectively.

which belong to the C_{2h} point group (C2/m space group). The Ge$_2$PAs structure adheres to the general electron counting rule, with germanium (Ge) atoms displaying fourfold coordination, while phosphorus (P) and arsenic (As) atoms exhibit threefold coordination. This coordination pattern is achieved through sp^3 hybridization, underlying the specific geometric arrangement of orbitals in the material. As shown in Fig. 1(a), the rectangular unit cell of Ge$_2$PAs consists of 12 Ge, 6 P, and 6 As atoms. The optimized lattice constants are a = 3.70 Å and b = 21.59 Å. The thermodynamic, mechanical, vibrational, and thermal stabilities have been previously demonstrated through cohesive energy analysis, phonon-dispersion calculations, and molecular dynamics simulations.[35] Considering the experimental progress on 2D Ge-based binary structures[17,19] and 2D Janus materials,[26,27] the realization of Ge$_2$PAs monolayers and their integration into 2D heterostructures can be anticipated.

The investigation of the electronic properties of materials is of profound significance, representing the foundational framework for the strategic design and optimization of materials tailored for electronic devices. In this respect, our attention now turns toward the analysis of the electronic characteristics of the monolayer. Figure 2 illustrates the electronic band structure of the Ge$_2$PAs monolayer, computed using GGA-PBE and HSE06 methods. The determined bandgap values are 1.55 and 2.23 eV for PBE and HSE calculations, respectively. Given the potential impact of spin–orbit coupling (SOC) on the band structure, we also examined the band structures
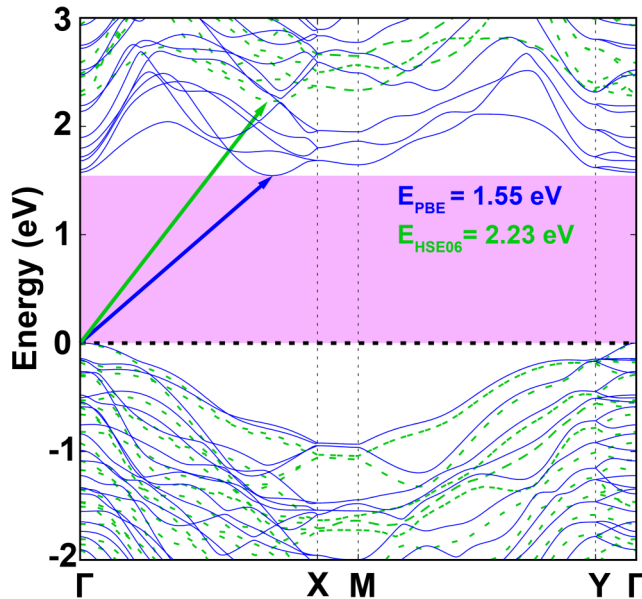
FIG. 2. The electronic band structure of a Ge$_2$PAs monolayer. The results for PBE and HSE06 are shown with solid blue and dashed green lines, respectively. The Fermi level is set to zero.

of the monolayer with SOC, as shown in Fig. S1 of the supplementary material. The results indicate that SOC exerted only a minimal influence on the calculated band structure, with no significant alteration to the characteristics and shapes of the electronic bands. The observed variations in the dispersion profiles along the $\Gamma - x$ and $\Gamma - y$ directions near the Fermi level indicate notable in-plane anisotropy. This anisotropy, evident in dispersion profiles, is underscored by the quantitative evidence from mobility values

reported in our previous study,[35] where electron and hole mobilities in the x-direction have been found to be much higher than those in the y-direction.

B. Electronic transport properties

Acknowledging the fundamental importance of 2D semiconductors in modern technology, a comprehensive understanding of electronic properties and their direct correlation with transport properties is pivotal for advancing current technologies. Considering the anisotropic electronic properties of a 2D Janus Ge$_2$PAs monolayer, we investigated its transport properties by focusing on the high-mobility direction as the preferred transport axis. In addition to its low carrier mobility, the y-direction also exhibits a significantly larger lattice constant ($b = 21.59$ Å). As a result, achieving proper electrostatic screening in this direction requires device lengths that exceed the ballistic transport regime. Therefore, we limited our analysis to the x-direction. Figure 3 illustrates the schematic design of a two-probe MSM nanodevice used in our simulations. In this schematic, the pink-shaded areas represent the left and right electrodes, while the unshaded area depicts the channel region. The setup involves connecting a left and right semi-infinite electron reservoir through a central region that encompasses the interfaces under consideration.

The contact interface between a semiconductor and its external metallic electrodes is crucial for both device performance and the accurate assessment of the material's transport properties.[48] The interface characteristics are primarily governed by the SB, which represents the difference between the metal's work function and the electron affinity of the semiconductor. This difference creates an energy barrier that hinders the flow of charges between the semiconductor and the metal.[49] While SB can provide useful rectifying properties and enable high-speed switching in certain systems, in some cases, the presence of an SB is undesirable due to its association with increased energy consumption and the complications it poses in directly examining the intrinsic characteristics of
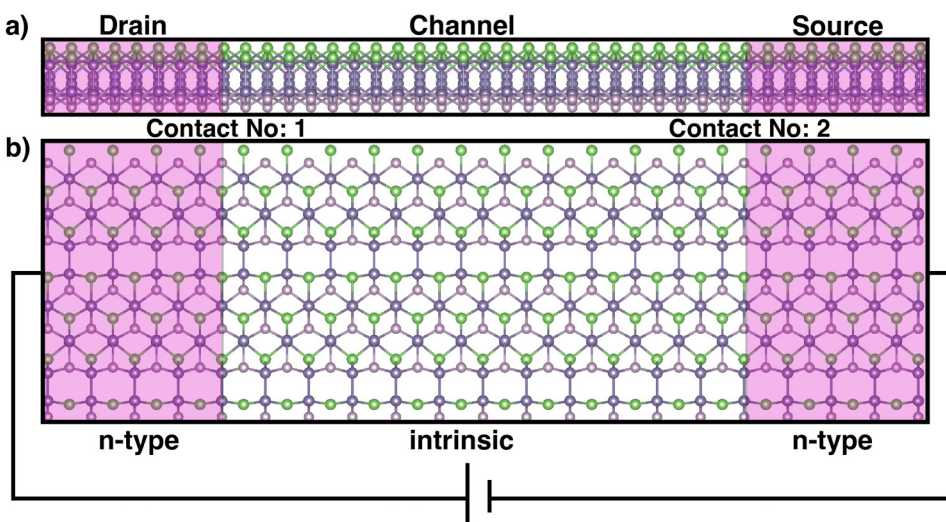

FIG. 3. Schematic diagrams of the two-probe configuration in (a) a side view and (b) a top view. Germanium, phosphorus, and arsenic atoms are presented as purple, pink, and green spheres, respectively.

semiconductor materials, especially for 2D semiconductor devices.[48] Thus, within semiconductor device engineering, achieving low SB values or Ohmic contact remains a central goal to reduce energy consumption and extend device lifespan. Common contact types typically consist of three main configurations: top contact, side contact, and vdW contact. However, these contacts often create challenges in achieving Ohmic or low SB behavior in real devices due to the presence of defects, vdW gaps, and manufacturing difficulties. To address these challenges, a novel type of configuration called atomic-level seamless contact has been developed.[50] This approach involves directly connecting low-dimensional metals and semiconductors with native chemical bonds, resulting in a contact that mitigates factors, such as lattice mismatch between different materials, and ensures a consistent and homogeneous environment for evaluating transport properties.

We adopted a strategy commonly found in the literature,[21,51–56] utilizing intrinsic 2D Ge_2PAs as the channel material while employing highly doped Ge_2PAs for both electrodes. In this respect, we employed the electrostatic doping method, which involves introducing localized charges that are individually attached to each atom.[45,57] This method has been demonstrated experimentally and has been shown to achieve electrically tunable doping levels of up to 10^{14} cm^{-2} in ultra-thin TMDs.[58] It is important to note that the structural stability is maintained under electrostatic doping, and the overall band structure, aside from the expected Fermi level shift, remains essentially unaltered as shown in Fig. S12 of the supplementary material. This assumption is supported by experimental evidence obtained from two-terminal graphene devices.[59]

When the metallicity of the electrodes is ensured through doping, the resulting structure can be simplified into an MSM configuration. An MSM structure essentially consists of two back-to-back Schottky contacts.[60] Each metal–semiconductor junction forms an SB due to the work function difference between the metal and the semiconductor. This arrangement is crucial for controlling the current flow through the device. Under an applied voltage, the two contacts exhibit different behaviors. Contact No. 1 undergoes a reverse bias, where the voltage enhances the SB and hinders charge carrier injection from a metal to a semiconductor. Conversely, Contact No. 2 experiences a forward bias, where the voltage reduces the SB and facilitates charge carrier injection. This differential biasing of the two contacts creates a potential difference across the semiconductor layer, driving the flow of current. By manipulating the SB heights through controlled biasing, MSM devices enable modulation of charge carrier transport and, consequently, the device's electronic characteristics.

In our investigation of the transport properties within the 2D Janus Ge_2PAs structure, we considered a range of electrode doping concentrations to mimic metallic electrodes with different work functions. Since the work function of a material directly depends on factors, such as density of states (DOS), temperature, carrier density, and doping concentration,[61] adjusting these parameters can emulate the characteristics of various metallic materials. In the present case, the selected doping concentrations for the electrodes are 0.015, 0.045, and 0.075 e/atom, corresponding to 4.51×10^{13}, 1.35×10^{14}, and 2.25×10^{14} cm^{-2}, respectively, which fall within experimentally achievable limits.[58] At the first concentration level,

the Ge_2PAs electrodes begin to exhibit metallic properties. At the second and third concentrations, they represent scenarios of moderate and heavy doping, respectively.[62,63] Under these conditions, the Fermi level of the electrodes is shifted 0.02, 0.16, and 0.24 eV above the conduction band minimum. Furthermore, we systematically investigated three channel lengths: 3.0, 4.5, and 6.5 nm at each doping level, aiming to identify the shortest possible sub-10 nm device configuration. Additionally, we also considered heavier doping concentrations of 3.16×10^{14} cm^{-2} and 6.01×10^{14} cm^{-2} for the longest case. This exploration was designed to elucidate how variations in the channel length and the doping concentration influence the electronic transport properties of the Janus Ge_2PAs-based MSM devices.

To investigate ballistic transport in devices with the specified parameters, we began by calculating the transmission spectra under equilibrium (0 V) and non-equilibrium conditions (0.5 and 1 V). The complete set of results is presented in Figs. S2, S3, and S4 of the supplementary material for bias voltages of 0, 0.5, and 1 V, respectively. Each figure employs a consistent layout: the plots from left to right within rows correspond to devices with increasing doping concentrations at a constant channel length, while plots from top to bottom within the columns belong to devices with increasing channel length at a constant doping concentration. In the transmission spectra for a 0 V bias, red dashed lines denote the Fermi level of the device. Similarly, for biased cases, red and green dashed lines represent the Fermi levels of the right and left electrodes, respectively.

We selected the results of the longest device (channel length of 6.5 nm) as the representative case to discuss the physical picture in the remainder of the paper. Transmission spectra of the 6.5 nm device under bias voltages of 0, 0.5, and 1 V are shown in Fig. 4. Similar to the figures in the supplementary material, plots progress from left to right for increasing doping concentration. At zero bias, the transmission spectra exhibit a transmission gap, indicative of the semiconducting nature of the channel. The width of this gap is influenced by electrode doping, with a slight increase observed for higher doping levels. When a finite bias is applied, transmission within the bias window becomes evident, which signifies the presence of current flow through the device. The inset of Fig. 4 further demonstrates that the transmission probability within the bias window is enhanced with increasing bias voltage. Additionally, a positive correlation is observed between electrode doping concentration and the overall transmission values.
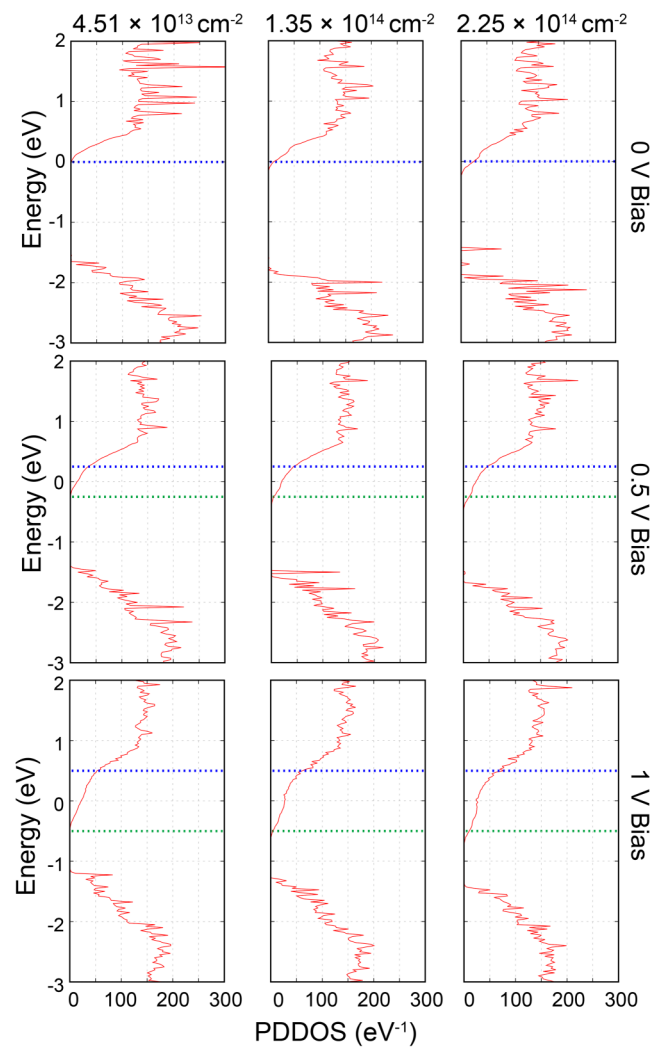
To elucidate the origin of the observed transmission values and their dependence on the applied bias, we calculated the bias-dependent projected device density of states (PDDOS). The complete set of results for bias voltages of 0, 0.5, and 1 V is presented in Figs. S5, S6, and S7 of the supplementary material, respectively. These figures maintain the same organizational layout as the provided transmission spectra data in the supplementary material. The blue dashed lines at 0 V of PDDOS plots indicate the device's Fermi level. Similarly, for biased cases, the blue and green dashed lines represent the Fermi levels of the right and left electrodes, respectively. The results for a 6.5 nm device under different biases are shown in Fig. 5. A strong correlation is observed between the PDDOS pattern and the previously discussed transmission spectra. Both diagrams for the devices in equilibrium conditions (0 V bias)
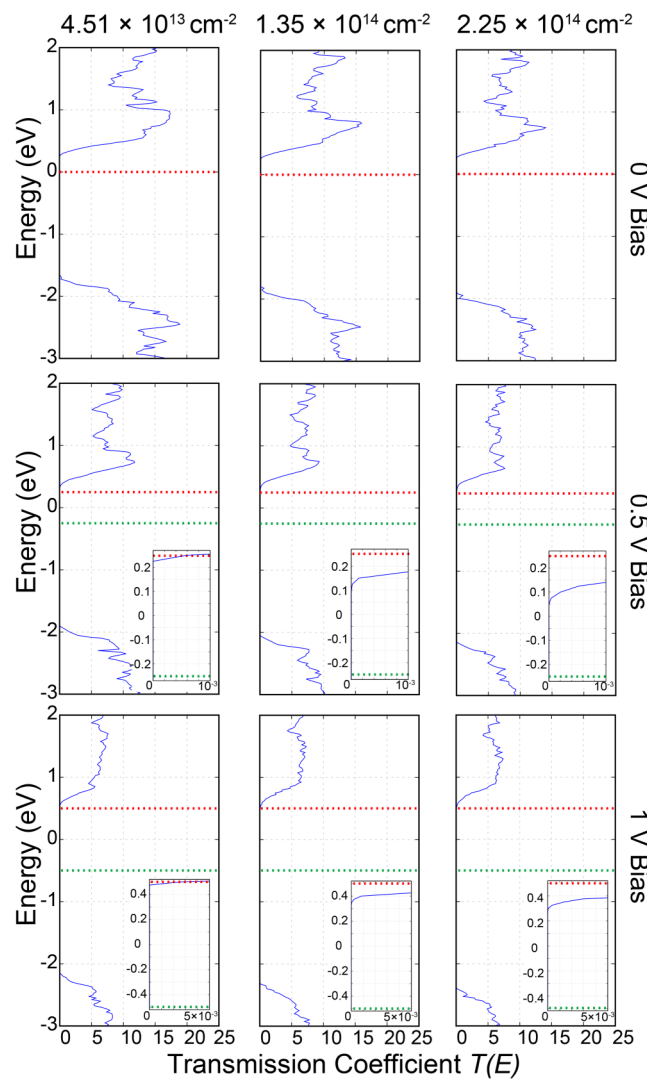
FIG. 4. Transmission spectra of devices with 6.5 nm channel length and 4.51×10^{13}, 1.35×10^{14}, and 2.25×10^{14} cm^{-2} under 0, 0.5, and 1 V biases. In the first row (0 V bias), red dashed lines indicate the Fermi level of the devices. In biased cases, the red and green dashed lines represent the Fermi levels of the right and left electrodes, respectively.

FIG. 5. Projected device density of states (PDDOS) of devices with 6.5 nm channel length and 4.51×10^{13}, 1.35×10^{14}, and 2.25×10^{14} cm^{-2} under 0, 0.5, and 1 V biases. In the first row (0 V bias), blue dashed lines indicate the Fermi level of the devices. In biased cases, the blue and green dashed lines represent the Fermi levels of the right and left electrodes, respectively.

depict a wide energy range around the Fermi level with low PDDOS values, signifying the semiconducting nature of the Janus Ge$_2$PAs monolayer. Under a finite bias, a non-zero DOS emerges within the bias window. Within this window, regions with the highest DOS contribute most significantly to the overall transmission observed in the system, facilitating the current flow through the device. The observed correlation between the higher transmission values and the increased electrode doping concentration can be attributed to the corresponding rise in the DOS across the device. This enhancement in the DOS directly influences the electronic behavior of the device. Moreover, the bias level effectively

amplifies the DOS within the bias window, further increasing the availability of electronic states for transmission.

We proceeded to examine the I–V characteristics of the modeled devices at 300 K. For these calculations, the applied bias voltage was swept across two electrodes within the range of −1 to +1 V, in increments of 0.1 V. To ensure computational efficiency and convergence, the density matrix obtained from each previous bias step was used as the initial guess for the subsequent calculation. The resulting I–V curves are presented in Figs. 6 and S10 of the supplementary material. The I–V curves exhibit a noticeable symmetry in the forward and reverse currents across various applied bias voltages, consistent with the design of symmetrical
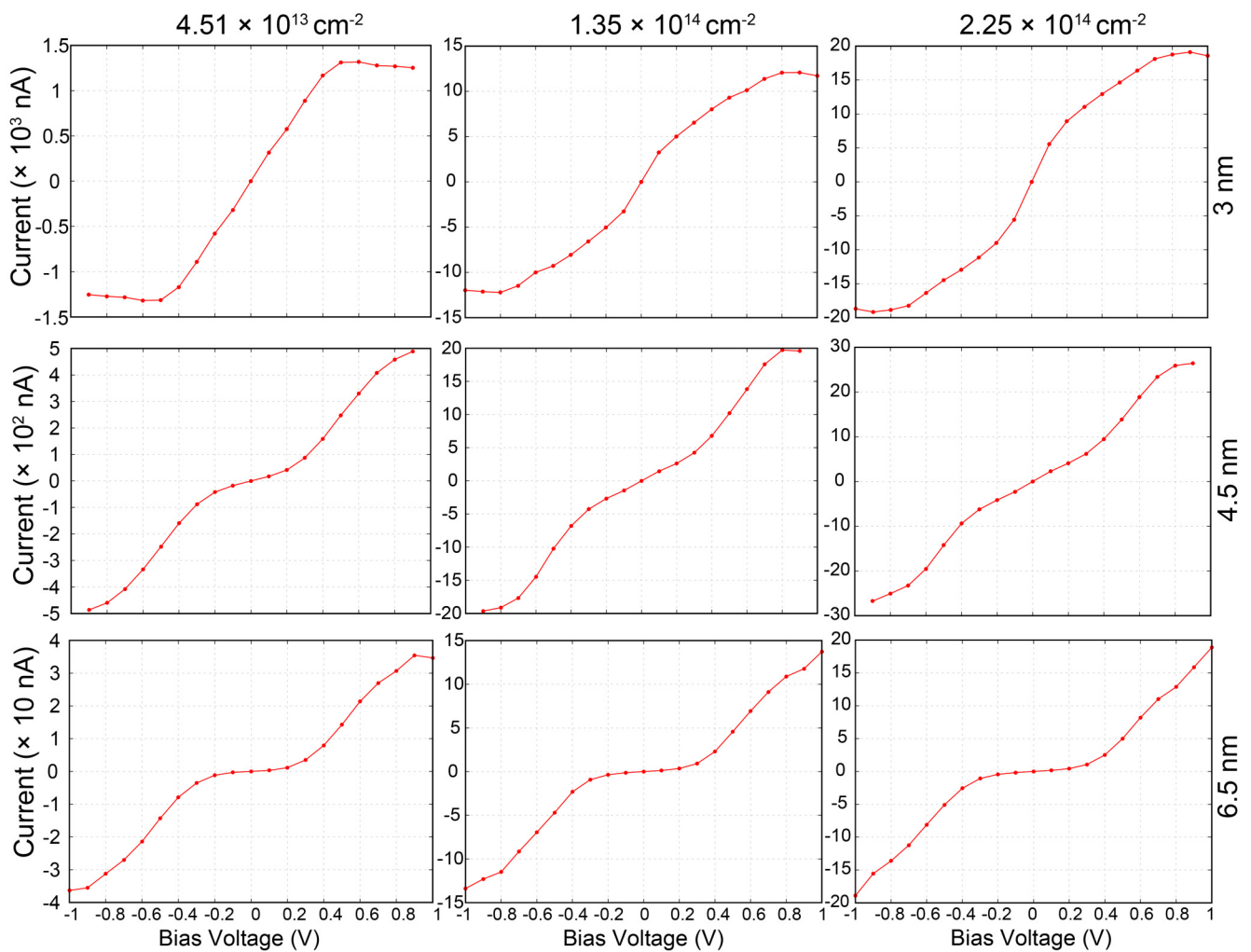
FIG. 6. Computed I–V characteristic curves of Ge$_2$PAs devices with increasing electrode doping concentration from left to right. The first row displays the I–V curves for a channel length of 3 nm, the second row for 4.5 nm, and the third row for 6.5 nm.

electrodes in the MSM configuration. However, an apparent deviation is observed for the device with 3 nm channel length, which exhibits significantly higher current levels. To elucidate this behavior, we calculated the Hartree Difference Potential (HDP) and its spatial derivative along the transport direction at a 0 V bias for all device configurations, as provided in Figs. S8 and S13 of the supplementary material. In the NEGF formalism, it is crucial for the electrostatic potential to reach equilibrium and becomes flat before reaching the electrode boundary. However, the shortest device configuration does not satisfy this criterion. Furthermore, while the HDP profile improves for devices with 4.5 nm channel length, they still exhibit high current in the low bias region, which deviates from the expected behavior for a semiconducting channel. Consequently, it is determined that the shortest operable device should have a channel length of 6.5 nm, aligning with typical

behavior observed in theoretical and experimental studies of MSM devices.[64,65] Furthermore, while the observed trends suggest a transition from coherent ballistic transport to electrostatic breakdown governed by channel length and doping concentration, defining a quantitative threshold remains challenging within the scope of the coherent NEGF framework.

Additionally, increasing the electrode doping concentration leads to considerable enhancement in the current values. This result aligns with the Landauer–Büttiker formula, which suggests that the magnitude of the current can be accurately calculated by integrating the area of transmission spectra within the bias window. The observed non-linearity in the I–V curves suggests that the electrical behavior at the metal–semiconductor interface is predominantly governed by the SB. To provide additional insight, we calculated the differential conductance, $G = dI/dV$, for the 6.5 nm
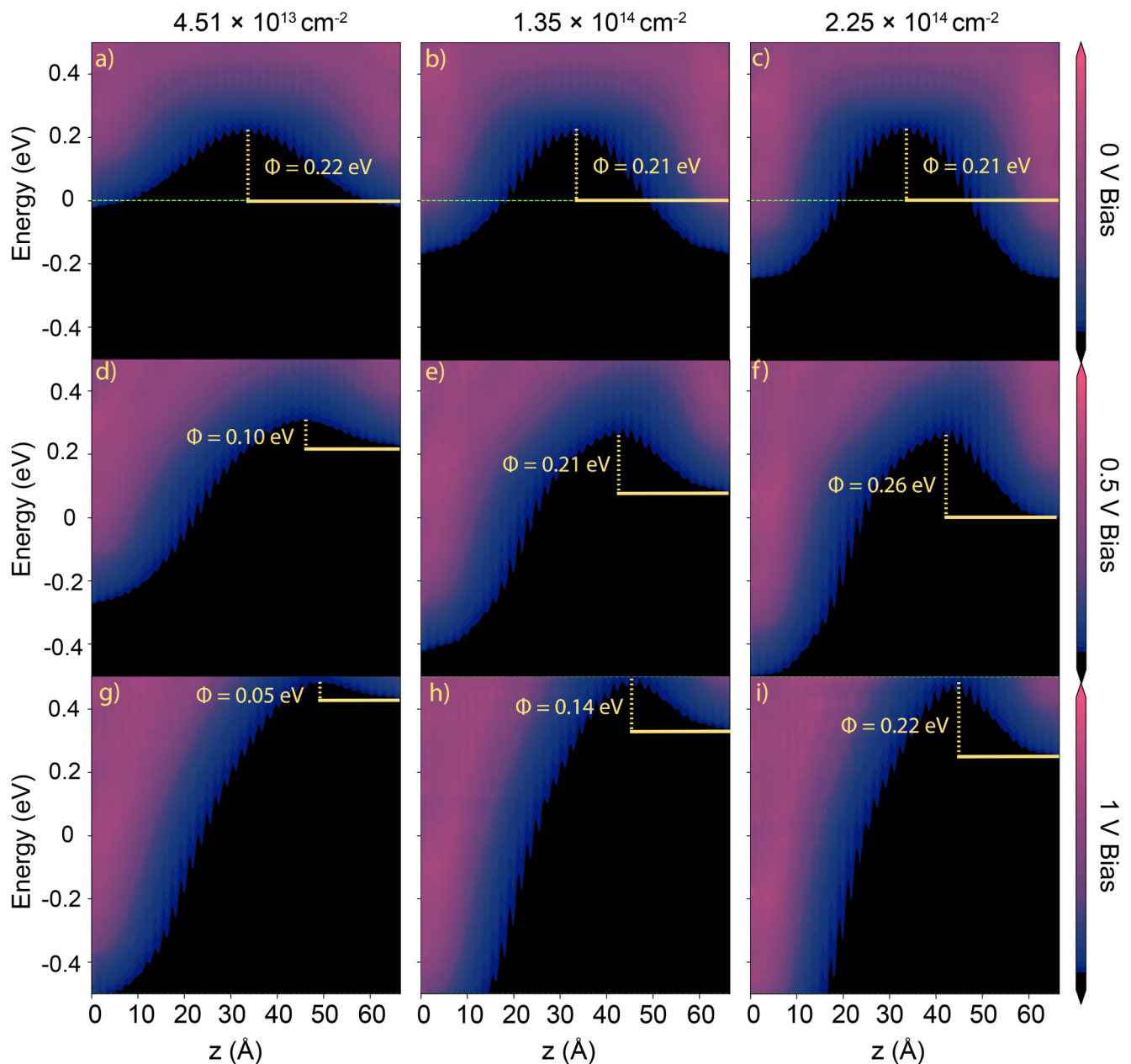
FIG. 7. Schottky barrier heights of devices with 6.5 nm channel length under (a)–(c) 0, (d)–(f) 0.5, and (g)–(i) 1 V bias.

MSM device with an electrode doping concentration of 2.25×10^{14} cm^{-2}. As shown in Fig. S14 of the supplementary material, the resulting dI/dV curve exhibits a minimum near zero bias, indicating suppressed carrier injection due to the SB, followed by a monotonic increase at higher biases. This trend is consistent with enhanced tunneling and thermionic emission as the barrier width and height are reduced with increasing bias. Such behavior

serves as a useful proxy for characterizing bias-dependent contact resistance under ideal ballistic conditions. Additionally, for this configuration, the off-state (I_{off}) and on-state (I_{on}) currents are calculated to be 3.9×10^{-11} and 1.9×10^{-7} A, respectively, resulting in an on/off ratio of $\sim 4.9 \times 10^{3}$, also illustrated in Fig. S15 of the supplementary material. This level of performance is regarded as adequate for applications, including low-power switching circuits,

sensing devices, and early-stage prototype designs, where a moderate on/off ratio combined with pronounced SB modulation can provide sufficient signal contrast for device functionality.[66–68]

Finally, to address the possible impact of p-type doping, we performed additional calculations using the longest device configuration and the highest doping concentration. The results reveal that the transport behavior under p-type doping is nearly identical to that observed for n-type doping (Fig. S11 in the supplementary material). This similarity extends to trends in the current magnitude and overall transport characteristics, which are in line with the intrinsic properties of the material. As demonstrated in our previous study,[35] the hole mobility of the 2D Ge_2PAs is comparable to its electron mobility along the high-mobility direction. This equivalence in carrier mobility explains the observed similarities in transport behavior between p-type and n-type doping scenarios.

To understand the role of the Schottky mechanism in devices with 6.5 nm channel length, we analyzed how the SB height (SBH) varies with the applied bias and doping concentration. Projected local density of states (PLDOS) calculations were performed at zero and finite bias voltages for different doping levels. PLDOS offers a comprehensive view of the device band diagram, facilitating detailed analysis of the SB. The SBH is determined by the energy difference between the Fermi level of the metal and the conduction band minimum (CBM) of the semiconductor at the metal–semiconductor interface. Under equilibrium conditions (zero bias), this energy difference can be equivalently expressed as the difference between the metal's work function and the semiconductor's electron affinity. When a bias is applied, the SBH is estimated by the energy difference between the CBM of the metallic electrode and the CBM of the semiconductor region.[56] The complete set of results is presented in Fig. S9 of the supplementary material and Fig. 7, where the latter specifically highlights the conduction band edges for a clearer depiction of the SBH values. Different colors represent absolute values of the DOS, with the intensity increasing from black to red, as indicated by the color bars on the right-hand side.

Figures 7(a)–7(c) depict the PLDOS under equilibrium (zero bias) conditions for varying doping levels. These results demonstrate that increasing the electrode doping concentration leads to a shift of the Fermi level (green dashed lines) toward higher energies within the conduction band. However, the SBH itself remains unaffected at zero bias. In contrast, the SBH increases with doping under finite bias conditions, as shown in Figs. 7(d)–7(i) for voltages 0.5 and 1 V, respectively. For devices with low doping concentration, the SBH exhibits a decrease with increasing bias voltage. This behavior facilitates easier transport of charge carriers across the barrier. However, this trend is not observed at medium and high doping levels. This can be attributed to narrowing of the depletion region with higher doping, leading to more stable barrier height.[69] Additionally, we found that for each bias value, the SB width decreases with increasing doping concentration. Since tunneling probability increases with reduced spatial distance, the higher doping level of the electrodes leads to enhanced tunneling current. Given the high current observed at elevated bias levels and the concurrent increase in SBH, which inhibits thermionic emission, it can be inferred that tunneling becomes the dominant transport mechanism as the bias voltage increases. It should also be noted that SB

height and width can be modulated by external factors, such as strain engineering, which results in significant current enhancement across all bias voltages, as demonstrated in Fig. S16 of the supplementary material.

IV. CONCLUSION

In this study, we thoroughly investigated the electronic transport properties of the 2D Janus Ge_2PAs monolayer, demonstrating its potential as a channel material in MSM (metal–semiconductor-metal) devices. Our calculations revealed the distinct electronic characteristics of the Janus Ge_2PAs monolayer, including its anisotropic, quasi-direct band structure and the negligible spin–orbit coupling (SOC) effect. By simulating a range of electrode doping concentrations and channel lengths, we systematically explored their impact on device performance. The results indicate that a minimum channel length of 6.5 nm is necessary for a device to exhibit typical MSM behavior. Furthermore, the doping concentration of the electrodes significantly influences the current values. Higher doping levels lead to enhanced currents due to an increased density of states (DOS) and more efficient tunneling current facilitated by a reduced SB width. We further examined the SB height (SBH) under different bias conditions and doping concentrations. While the SBH remains constant at equilibrium with increased doping, it increases under a finite bias, influencing charge carrier transport. The dominance of tunneling current at higher biases underscores the critical role of electrode doping in optimizing device performance. This comprehensive analysis provides valuable insights into the design and optimization of 2D Janus Ge_2PAs-based MSM devices. Our findings contribute to the broader understanding of electronic transport in 2D materials and pave the way for future experimental and theoretical investigations in the field of nanoelectronics.

SUPPLEMENTARY MATERIAL

See the supplementary material for the electronic band structure of a Ge_2PAs monolayer with SOC; the transmission spectra and the projected density of states of devices of 3, 4.5, and 6.5 nm channel length under 0, 0.5, and 1 V bias voltages; the projected local density of states of devices with 6.5 nm channel length; I–V characteristic curves for higher doping concentrations and p-type doping; band structures and PDOS of undoped and n-type doped Ge_2PAs monolayers; Hartree difference potential and its derivative along the transport direction; differential conductance as a function of bias voltage; an on/off current ratio of 6.5 nm MSM device; and PLDOS for the 6.5 nm MSM device under 4% tensile strain and corresponding I–V characteristics.

ACKNOWLEDGMENTS

09 December 2025 11:57:19

AUTHOR DECLARATIONS

Conflict of Interest

The authors have no conflicts to disclose.

Author Contributions

D. H. Ozbey: Formal analysis (equal); Investigation (lead); Methodology (lead); Writing – original draft (equal); Writing – review & editing (equal). **G. Ö. Sargin:** Formal analysis (equal); Investigation (equal); Methodology (equal); Writing – original draft (supporting). **V. Ongun Özçelik:** Formal analysis (supporting); Supervision (supporting); Writing – original draft (supporting); Writing – review & editing (supporting). **E. Durgun:** Conceptualization (lead); Formal analysis (equal); Supervision (lead); Writing – original draft (equal); Writing – review & editing (equal).

DATA AVAILABILITY

The data that support the findings of this study are available within the article and its supplementary material.

REFERENCES

[1] C. E. Leiserson, N. C. Thompson, J. S. Emer, B. C. Kuszmaul, B. W. Lampson, D. Sanchez, and T. B. Schardl, "There's plenty of room at the top: What will drive computer performance after Moore's law?" Science **368**, eaam9744 (2020).

[2] S. Wang, X. Liu, and P. Zhou, "The road for 2D semiconductors in the silicon age," Adv. Mater. **34**, 2106886 (2022).

[3] W. Cao, H. Bu, M. Vinet, M. Cao, S. Takagi, S. Hwang, T. Ghani, and K. Banerjee, "The future transistors," Nature **620**, 501 (2023).

[4] D. Akinwande, C. Huyghebaert, C.-H. Wang, M. I. Serna, S. Goossens, L.-J. Li, H.-S. P. Wong, and F. H. Koppens, "Graphene and two-dimensional materials for silicon technology," Nature **573**, 507 (2019).

[5] X. Huang, C. Liu, and P. Zhou, "2D semiconductors for specific electronic applications: From device to system," npj 2D Mater. Appl. **6**, 51 (2022).

[6] S. Ahmed and J. Yi, "Two-dimensional transition metal dichalcogenides and their charge carrier mobilities in field-effect transistors," Nano Micro Lett. **9**, 50 (2017).

[7] Y. K. Hong, N. Liu, D. Yin, S. Hong, D. H. Kim, S. Kim, W. Choi, and Y. Yoon, "Recent progress in high-mobility thin-film transistors based on multilayer 2D materials," J. Phys. D: Appl. Phys. **50**, 164001 (2017).

[8] H. Li, J.-K. Huang, Y. Shi, and L.-J. Li, "Toward the growth of high mobility 2D transition metal dichalcogenide semiconductors," Adv. Mater. Interfaces **6**, 1900220 (2019).

[9] H. Song, J. Liu, B. Liu, J. Wu, H.-M. Cheng, and F. Kang, "Two-dimensional materials for thermal management applications," Joule **2**, 442 (2018).

[10] M. Chhowalla, D. Jena, and H. Zhang, "Two-dimensional semiconductors for transistors," Nat. Rev. Mater. **1**, 16052 (2016).

[11] S.-L. Li, K. Tsukagoshi, E. Orgiu, and P. Samorì, "Charge transport and mobility engineering in two-dimensional transition metal chalcogenide semiconductors," Chem. Soc. Rev. **45**, 118 (2016).

[12] C. Zhang, R. Wang, H. Mishra, and Y. Liu, "Two-dimensional semiconductors with high intrinsic carrier mobility at room temperature," Phys. Rev. Lett. **130**, 087001 (2023).

[13] H. Huang, X. Fan, D. J. Singh, and W. Zheng, "Recent progress of TMD nanomaterials: Phase transitions and applications," Nanoscale **12**, 1247 (2020).

[14] Z. Lin, B. R. Carvalho, E. Kahn, R. Lv, R. Rao, H. Terrones, M. A. Pimenta, and M. Terrones, "Defect engineering of two-dimensional transition metal dichalcogenides," 2D Mater. **3**, 022002 (2016).

[15] H. Sar, J. Gao, and X. Yang, "2D layered SiP as anisotropic nonlinear optical material," Sci. Rep. **11**, 6372 (2021).

[16] D. Kim, K. Park, J. H. Lee, I. S. Kwon, I. H. Kwak, and J. Park, "Anisotropic 2D SiAs for high-performance UV–visible photodetectors," Small **17**, 2006310 (2021).

[17] L. Li, W. Wang, P. Gong, X. Zhu, B. Deng, X. Shi, G. Gao, H. Li, and T. Zhai, "2D GeP: An unexploited low-symmetry semiconductor with strong in-plane anisotropy," Adv. Mater. **30**, 1706771 (2018).

[18] D. Kim, K. Park, F. Shojaei, T. T. Debela, I. S. Kwon, I. H. Kwak, J. Seo, J. P. Ahn, J. Park, and H. S. Kang, "Thickness-dependent bandgap and electrical properties of GeP nanosheets," J. Mater. Chem. A **7**, 16526 (2019).

[19] C. S. Jung, D. Kim, S. Cha, Y. Myung, F. Shojaei, H. G. Abbas, J. A. Lee, E. H. Cha, J. Park, and H. S. Kang, "Two-dimensional GeAs with a visible range band gap," J. Mater. Chem. A **6**, 9089 (2018).

[20] A.-Q. Cheng, Z. He, J. Zhao, H. Zeng, and R.-S. Chen, "Monolayered silicon and germanium monopnictide semiconductors: Excellent stability, high absorbance, and strain engineering of electronic properties," ACS Appl. Mater. Interfaces **10**, 5133 (2018).

[21] P. Li, W. Wu, Y. Xu, J. Liu, S. Wu, Y. Ye, C. Liang, and X. C. Zeng, "Two-dimensional IV–V monolayers with highly anisotropic carrier mobility and electric transport properties," J. Phys. Chem. Lett. **12**, 1058 (2021).

[22] S. Zhang, S. Guo, Y. Huang, Z. Zhu, B. Cai, M. Xie, W. Zhou, and H. Zeng, "Two-dimensional SiP: An unexplored direct band-gap semiconductor," 2D Mater. **4**, 015030 (2017).

[23] D. Ozbey and M. Kilic, "Investigation of anisotropic mechanical, electronic, and charge carrier transport properties of germanium-pnictogen monolayers," J. Phys. D: Appl. Phys. **55**, 185302 (2022).

[24] H. Zeng, T.-C. Zhang, H.-G. Bao, J. Zhao, and D.-Z. Ding, "Influences of point defects on electron transport of two-dimensional GeP semiconductor device," Nanotechnology **34**, 185204 (2023).

[25] H. Zeng, T.-C. Zhang, H.-G. Bao, J. Zhao, and D.-Z. Ding, "Computational design of two-dimensional GeP based flexible strain sensor: Distinct JV response," Sens. Actuators A: Phys. **351**, 114155 (2023).

[26] J. Zhang, S. Jia, I. Kholmanov, L. Dong, D. Er, W. Chen, H. Guo, Z. Jin, V. B. Shenoy, L. Shi et al., "Janus monolayer transition-metal dichalcogenides," ACS Nano **11**, 8192 (2017).

[27] A.-Y. Lu, H. Zhu, J. Xiao, C.-P. Chuu, Y. Han, M.-H. Chiu, C.-C. Cheng, C.-W. Yang, K.-H. Wei, Y. Yang et al., "Janus monolayers of transition metal dichalcogenides," Nat. Nanotechnol. **12**, 744 (2017).

[28] R. Li, Y. Cheng, and W. Huang, "Recent progress of Janus 2D transition metal chalcogenides: From theory to experiments," Small **14**, 1802091 (2018).

[29] L. Zhang, Z. Yang, T. Gong, R. Pan, H. Wang, Z. Guo, H. Zhang, and X. Fu, "Recent advances in emerging Janus two-dimensional materials: From fundamental physics to device applications," J. Mater. Chem. A **8**, 8813 (2020).

[30] M. Yagmurcukardes, Y. Qin, S. Ozen, M. Sayyad, F. M. Peeters, S. Tongay, and H. Sahin, "Quantum properties and applications of 2D Janus crystals and their superlattices," Appl. Phys. Rev. **7**, 011311 (2020).

[31] K. Ren, K. Wang, Y. Luo, M. Sun, T. Altalhi, B. I. Yakobson, and G. Zhang, "Ultralow frequency interlayer mode from suppressed van der Waals coupling in polar Janus SMoSe/SWSe heterostructure," Mater. Today Phys. **53**, 101689 (2025).

[32] M. Sun and U. Schwingenschlogl, "B₂P₆: A two-dimensional anisotropic Janus material with potential in photocatalytic water splitting and metal-ion batteries," Chem. Mater. **32**, 4795 (2020).

[33] J. Schmeink, J. Osterfeld, O. Kharsah, S. Sleziona, and M. Schleberger, "Unraveling the influence of defects in Janus MoSSe and Janus alloys MoS₂(₁₋ₓ)Se₂ₓ," npj 2D Mater. Appl. **8**, 67 (2024).

[34] M. Sayyad, J. Kopaczek, C. M. Gilardoni, W. Chen, Y. Xiong, S. Yang, K. Watanabe, T. Taniguchi, R. Kudrawiec, G. Hautier et al., "The defects genome of Janus transition metal dichalcogenides," Adv. Mater. **36**, 2403583 (2024).

[35]D. Ozbey, M. Kilic, and E. Durgun, "Two-dimensional Janus GePAs monolayer: A direct-band-gap semiconductor with high and anisotropic mobility for efficient photocatalytic water splitting," Phys. Rev. Appl. **17**, 034043 (2022).

[36]J. Qiao, X. Kong, Z.-X. Hu, F. Yang, and W. Ji, "High-mobility transport anisotropy and linear dichroism in few-layer black phosphorus," Nat. Commun. **5**, 4475 (2014).

[37]J. Yao and G. Yang, "2D material broadband photodetectors," Nanoscale **12**, 454 (2020).

[38]G. Kresse and J. Hafner, "*Ab initio* molecular dynamics for liquid metals," Phys. Rev. B **47**, 558 (1993).

[39]G. Kresse and J. Hafner, "*Ab initio* molecular-dynamics simulation of the liquid-metal–amorphous-semiconductor transition in germanium," Phys. Rev. B **49**, 14251 (1994).

[40]J. P. Perdew, K. Burke, and M. Ernzerhof, "Generalized gradient approximation made simple," Phys. Rev. Lett. **77**, 3865 (1996).

[41]P. E. Blöchl, "Projector augmented-wave method," Phys. Rev. B **50**, 17953 (1994).

[42]H. J. Monkhorst and J. D. Pack, "Special points for Brillouin-zone integrations," Phys. Rev. B **13**, 5188 (1976).

[43]S. Grimme, "Semiempirical GGA-type density functional constructed with a long-range dispersion correction," J. Comput. Chem. **27**, 1787 (2006).

[44]S. Smidstrup, T. Markussen, P. Vancraeyveld, J. Wellendorff, J. Schneider, T. Gunst, B. Verstichel, D. Stradi, P. A. Khomyakov, U. G. Vej-Hansen *et al.*, "QuantumATK: An integrated platform of electronic and atomic-scale modelling tools," J. Phys.: Condens. Matter **32**, 015901 (2020).

[45]M. Brandbyge, J.-L. Mozos, P. Ordejón, J. Taylor, and K. Stokbro, "Density-functional method for nonequilibrium electron transport," Phys. Rev. B **65**, 165401 (2002).

[46]M. J. Van Setten, M. Giantomassi, E. Bousquet, M. J. Verstraete, D. R. Hamann, X. Gonze, and G.-M. Rignanese, "The PseudoDojo: Training and grading a 85 element optimized norm-conserving pseudopotential table," Comput. Phys. Commun. **226**, 39 (2018).

[47]H. Haug A.-P. Jauho *et al.*, *Quantum Kinetics in Transport and Optics of Semiconductors* (Springer, 2008), Vol. 2.

[48]A. Allain, J. Kang, K. Banerjee, and A. Kis, "Electrical contacts to two-dimensional semiconductors," Nat. Mater. **14**, 1195 (2015).

[49]S. M. Sze, Y. Li, and K. K. Ng, *Physics of Semiconductor Devices* (John Wiley & Sons, 2021).

[50]S. Chen, S. Wang, C. Wang, Z. Wang, and Q. Liu, "Latest advance on seamless metal-semiconductor contact with ultralow Schottky barrier in 2D-material-based devices," Nano Today **42**, 101372 (2022).

[51]H. Qu, S. Guo, W. Zhou, B. Cai, S. Zhang, Y. Huang, Z. Li, X. Chen, and H. Zeng, "Electronic structure and transport properties of 2D RhTeCl: A NEGF-DFT study," Nanoscale **11**, 20461 (2019).

[52]Z. Ni, Q. Liu, K. Tang, J. Zheng, J. Zhou, R. Qin, Z. Gao, D. Yu, and J. Lu, "Tunable bandgap in silicene and germanene," Nano Lett. **12**, 113 (2012).

[53]W. Zhou, S. Zhang, S. Guo, Y. Wang, J. Lu, X. Ming, Z. Li, H. Qu, and H. Zeng, "Designing sub-10-nm metal-oxide-semiconductor field-effect transistors via ballistic transport and disparate effective mass: The case of two-dimensional BiN," Phys. Rev. Appl. **13**, 044066 (2020).

[54]J. Zhang, Y. Qin, W. Zhou, Y. Hu, C. Chen, J. Yang, H. Qu, and X. Hu, "Electronic properties and ballistic transport performances of 2D GaO: A DFT-NEGF study," ACS Appl. Electron. Mater. **5**, 5598 (2023).

[55]X. Hu, H. Qu, L. Xu, W. Liu, T. Guo, B. Cai, X. Yu, J. Zhu, and S. Zhang, "DFT coupled with NEGF study of the electronic properties and ballistic transport performances of 2D SbSiTe$_3$," Nanoscale **12**, 9958 (2020).

[56]W. Wu, D. Li, Y. Xu, and X. C. Zeng, "Two-dimensional GeC$_2$ with tunable electronic and carrier transport properties and a high current on/off ratio," J. Phys. Chem. Lett. **12**, 11488 (2021).

[57]D. Stradi, U. Martinez, A. Blom, M. Brandbyge, and K. Stokbro, "General atomistic approach for modeling metal-semiconductor interfaces using density functional theory and nonequilibrium Green's function," Phys. Rev. B **93**, 155302 (2016).

[58]Y. Wang, J. Xiao, H. Zhu, Y. Li, Y. Alsaid, K. Y. Fong, Y. Zhou, S. Wang, W. Shi, Y. Wang *et al.*, "Structural phase transition in monolayer MoTe$_2$ driven by electrostatic doping," Nature **550**, 487 (2017).

[59]P. V. Nguyen, N. C. Teutsch, N. P. Wilson, J. Kahn, X. Xia, A. J. Graham, V. Kandyba, A. Giampietri, A. Barinov, G. C. Constantinescu *et al.*, "Visualizing electrostatic gating effects in two-dimensional heterostructures," Nature **572**, 220 (2019).

[60]S. Sze, D. Coleman, Jr., and A. Loya, "Current transport in metal-semiconductor-metal (MSM) structures," Solid-State Electron. **14**, 1209 (1971).

[61]A. Kahn, "Fermi level, work function and vacuum level," Mater. Horiz. **3**, 7 (2016).

[62]P. Luo, F. Zhuge, Q. Zhang, Y. Chen, L. Lv, Y. Huang, H. Li, and T. Zhai, "Doping engineering and functionalization of two-dimensional metal chalcogenides," Nanoscale Horiz. **4**, 26 (2019).

[63]A. Grillo, A. Di Bartolomeo, F. Urban, M. Passacantando, J. M. Caridad, J. Sun, and L. Camilli, "Observation of 2D conduction in ultrathin germanium arsenide field-effect transistors," ACS Appl. Mater. Interfaces **12**, 12998 (2020).

[64]C.-H. Kuo, J.-M. Wu, S.-J. Lin, and W.-C. Chang, "High sensitivity of middle-wavelength infrared photodetectors based on an individual InSb nanowire," Nanoscale Res. Lett. **8**, 327 (2013).

[65]Z. Zhang, K. Yao, Y. Liu, C. Jin, X. Liang, Q. Chen, and L.-M. Peng, "Quantitative analysis of current–voltage characteristics of semiconducting nanowires: Decoupling of contact effects," Adv. Funct. Mater. **17**, 2478 (2007).

[66]C.-J. Shih, Q. H. Wang, Y. Son, Z. Jin, D. Blankschtein, and M. S. Strano, "Tuning on–off current ratio and field-effect mobility in a MoS$_2$–graphene heterostructure via Schottky barrier modulation," ACS Nano **8**, 5790 (2014).

[67]Y.-L. Hong, Z. Liu, L. Wang, T. Zhou, W. Ma, C. Xu, S. Feng, L. Chen, M.-L. Chen, D.-M. Sun *et al.*, "Chemical vapor deposition of layered two-dimensional MoSi$_2$N$_4$ materials," Science **369**, 670 (2020).

[68]Z. Li, J. Han, S. Cao, Z. Zhang, and X. Deng, "First-principles study of metal-semiconductor contacts and quantum transport simulations for 5.1-nm monolayer MoSi$_2$N$_4$ devices," Phys. Rev. Appl. **21**, 054062 (2024).

[69]A. Firrincieli, K. Martens, E. Simoen, C. Claeys, and J. Kittl, "Study of the impact of doping concentration and Schottky barrier height on ohmic contacts to n-type germanium," Microelectron. Eng. **106**, 129 (2013).

09 December 2025 11:57:19